

PEARL: Geometry Aligns Semantics for Training-Free Open-Vocabulary Semantic Segmentation

Gensheng Pei¹, Xiruo Jiang², Xinhao Cai³, Tao Chen³, Yazhou Yao³, Byeungwoo Jeon^{1*}

¹Department of Electrical and Computer Engineering, Sungkyunkwan University

²School of Computing and Artificial Intelligence, Southwest Jiaotong University

³School of Computer Science and Engineering, Nanjing University of Science and Technology

<https://github.com/PGSmall/PEARL>

Abstract

Training-free open-vocabulary semantic segmentation (OVSS) promises rapid adaptation to new label sets without retraining. Yet, many methods rely on heavy post-processing or handle text and vision in isolation, leaving cross-modal geometry underutilized. Others introduce auxiliary vision backbones or multi-model pipelines, which increase complexity and latency while compromising design simplicity. We present PEARL, Procrustes alignment with text-aware Laplacian propagation, a compact two-step inference that follows an align-then-propagate principle. The Procrustes alignment step performs an orthogonal projection inside the last self-attention block, rotating keys toward the query subspace via a stable polar iteration. The text-aware Laplacian propagation then refines per-pixel logits on a small grid through a confidence-weighted, text-guided graph solve: text provides both a data-trust signal and neighbor gating, while image gradients preserve boundaries. In this work, our method is fully training-free, plug-and-play, and uses only fixed constants, adding minimal latency with a small per-head projection and a few conjugate-gradient steps. Our approach, PEARL, sets a new state-of-the-art in training-free OVSS without extra data or auxiliary backbones across standard benchmarks, achieving superior performance under both with-background and without-background protocols.

1. Introduction

Open-vocabulary semantic segmentation [39, 45, 67, 72, 73, 77, 81] (OVSS) assigns a category to every pixel when the label set is specified at inference time through natural language. In the training-free setting, a frozen vision-language backbone provides dense visual features and text embed-

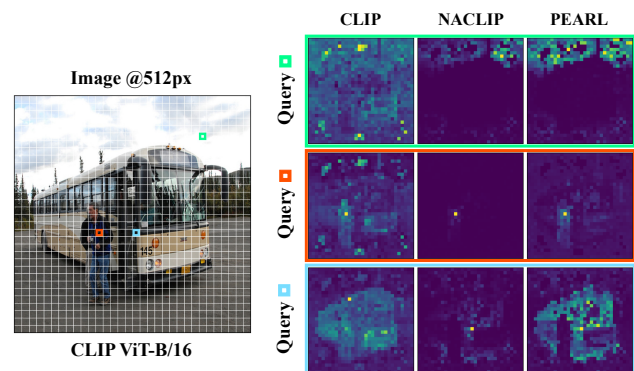


Figure 1. **Attention visualization at selected query points.** We show an input resized to 512×512 using the CLIP ViT-B/16 vision encoder. For each colored query, we compare the attention maps produced by CLIP [51], NACLIP [26], and our PEARL. CLIP exhibits diffuse and background-biased responses, while NACLIP improves localization but often fragments objects into isolated peaks. By performing Procrustes alignment in the last self-attention block, PEARL yields compact and object-consistent attention, suppresses background spill, and better preserves thin parts, resulting in stable focus with reduced grid artifacts.

dings, and masks are obtained by matching patches to text prototypes without any task-specific optimization [5, 32]. Early progress [7, 77] built on zero-shot scene parsing [47, 48] with word embeddings. The field accelerated with contrastive vision-language models (VLMs) such as CLIP [51] and ALIGN [27], paired with strong Transformer backbones like ViT [21, 41, 61] and the DINO family [9, 46, 58]. Supervised segmentation remains a touchstone for dense prediction quality, but OVSS aims to retain flexibility while avoiding retraining on every new label set.

Training-based approaches [16, 39, 67, 72] convert these ingredients into dense predictors by learning decoders, adding lightweight adapters, or leveraging weak supervision. Representative work attaches decoders to frozen or partially tuned backbones [37, 67, 72], adapts CLIP with mask-aware objectives or side modules [16, 39, 73], and

*Corresponding author.

exploits image labels, boxes, or captions to reduce mask annotation [10, 25, 38, 69–71, 78, 82]. A complementary line distills object-centric structure from self-supervised ViTs into CLIP-like architectures to inject stronger grouping cues [5, 29, 66]. These routes can reach high accuracy, but require extra data and task-specific training.

In parallel, the training-free paradigm keeps backbones frozen, improving inference only. A pioneering baseline, MaskCLIP [81], computes cosine similarity between dense CLIP features and text prompts. Subsequent work strengthens this recipe along three directions. First, feature purification and re-alignment suppress outliers, rebuild patch correlations, or select informative attention heads [6, 28, 36, 54, 74, 76]. Second, spatial refinement encourages coherence using classical mask refinement and neighbor-aware grouping [1, 26, 34, 60, 65]. Third, object and context priors are imported through spectral cues or multi-model assemblies, *e.g.*, distilling DINO-style structure [30, 35, 59] or leveraging visual context graphs [32]. These approaches can be practical, though heavy post-processing or auxiliary components may increase complexity and latency.

Two observations motivate our work. (i) Contrastive pretraining emphasizes global image-text agreement rather than dense prediction. Near the top of the vision encoder, a few background-dominated directions can steer token interactions, yielding patch geometry that is misaligned and spatially inconsistent for pixel-level decisions [36, 81]. When the geometry at the source is off, downstream smoothing treats symptoms rather than causes. (ii) Text is commonly used only as a classifier. It rarely governs how pixels exchange information, even though relations in the text space suggest which categories should reinforce one another and which should remain separate [26, 32]. These two points suggest a simple strategy: first correct the geometry where attention scores are formed, then propagate semantics with guidance from both text relations and image boundaries.

Following this strategy, we present PEARL, a Procrustes alignment with text-aware Laplacian propagation. The first step inserts an orthogonal Procrustes alignment into the last self-attention block. After weighted centering of queries and keys, a single input-dependent rotation aligns keys to the query subspace. This closed-form correction preserves magnitudes and angles while removing background-biased drift that destabilizes patch-text similarities. As shown in Fig. 1, attention maps at selected queries (using CLIP ViT-B/16) show that vanilla CLIP is diffuse and background-biased, while NAELIP [26] sharpens focus but fragments objects, our PEARL yields compact, object-consistent responses that preserve thin structures. This suggests that aligning keys to queries before scoring stabilizes token geometry and leads to cleaner masks. The second step refines the class-logit field on a compact grid using a text-aware Laplacian: a confidence-weighted data term trusts pixels

with reliable evidence, while a text agreement prior gates neighbor links according to semantic relatedness. Image gradients protect boundaries, ensuring that refinement respects edges [1, 34]. Unlike class-agnostic smoothing, text guides both the data trust and the edges. Unlike heavy spectral or multi-backbone assemblies, the refinement is a single linear solve with modest cost [32].

To summarize, our PEARL addresses the two weaknesses above at their origin with two principled operators. Procrustes alignment repairs token geometry exactly where attention is computed, and text-aware Laplacian propagation transforms language from a simple labeler into a structural prior that guides how evidence spreads across the image. The two parts work together: the first enhances what attention sees, and the second organizes how pixels align. Across standard OVSS benchmarks, the approach achieves coherent masks for small objects, stable coverage for “*stuff*” regions, and strong accuracy among training-free methods, all without auxiliary backbones or extra supervision.

2. Related Work

From Closed-Set to Open-Vocabulary Semantic Segmentation. Classical semantic segmentation [12, 42, 68], built on pixel-annotated datasets (*e.g.*, PASCAL VOC [23], MS COCO [40], ADE20K [79, 80], Cityscapes [17]), works well but is limited to a *closed set* of categories. Extending them to new concepts requires costly re-annotation and re-training. To overcome this, the field has shifted towards OVSS. Early steps toward open settings used word embeddings for zero-shot transfer [7, 77]. The move to open-vocabulary segmentation accelerated with the emergence of VLMs like CLIP [51] and ALIGN [27], which align images and text in a shared space. Yet CLIP is trained for global alignment, not dense prediction: patch features are often noisy and spatially imprecise. Most recent work, therefore, aims to recover spatially coherent, text-aware masks either by adapting the model with additional data or by reshaping the inference process. We take the latter route with our method, PEARL: a training-free, plug-and-play *align-then-propagate* scheme that first corrects *feature geometry* and then performs *text-aware propagation* entirely at inference. **Training-Based OVSS.** This family adapts pre-trained VLMs [24, 27, 49, 51] or VMs [9, 33, 46, 52] to produce dense masks, using additional data to fine-tune a decoder, add small adapters, or train with weak labels. Many methods reduce the gap to dense prediction by learning on task data. Some attach a decoder to frozen or partially tuned VLMs [37, 67, 72], others adapt CLIP via mask-aware training or lightweight adapters [16, 39, 73], and a broad line leverages weaker supervision from image labels, boxes, or captions [10, 25, 38, 69–71, 78, 82]. A complementary trend fuses foundation models: object-centric signals from self-supervised ViTs (*e.g.*, DINO [9, 46, 58]) are distilled or

aligned into CLIP [5, 29, 63, 66]. These approaches deliver strong accuracy but incur curation costs, training bias toward seen concepts, and additional compute requirements. By contrast, our proposed approach, PEARL, needs no extra training or data and runs parameter-free inference, combining an *orthogonal Procrustes alignment* in the last self-attention with a *text-aware Laplacian propagation* to keep the design simple while preserving generalization.

Training-Free OVSS. Training-free paradigm *does not train* anything new. It keeps backbones frozen and modifies only the inference procedure to obtain text-aware masks. A basic baseline computes cosine similarity between dense CLIP features and text prompts [81], then improves it along three directions. First, feature purification and re-alignment suppresses outlier/background tokens, rebuilds patch correlations, or selects informative attention heads [6, 13, 22, 28, 31, 50, 54, 74, 76], with recent work targeting class redundancy and vision-language ambiguity [13]. Second, spatial refinement with locality priors enforces coherence using mask refinement techniques [1, 34], grouping and count-aware propagation [43, 60, 65], or neighbor/feedback-aware attention mechanism [2–4, 15, 26, 75]. Third, object-context fusion imports structure from stronger vision backbones or multi-model pipelines (*e.g.*, DINO [9], Diffusion [53], SAM [33]) for correspondences, prototypes, or prompt-based refinement [3, 4, 35, 36, 56]. Previous methods are effective but often rely on multi-stage heuristics, intensive post-processing, or auxiliary backbones. In this work, we introduce PEARL, Procrustes alignment with text-aware Laplacian propagation, an *align-then-propagate* framework in which an *orthogonal Procrustes* step fixes attention geometry and a confidence-weighted, *text-guided Laplacian* refines logits on a small grid to yield coherent masks with a fully training-free, plug-and-play pipeline.

3. Method

3.1. Preliminaries: Training-free OVSS

Vision Encoder. Training-free open-vocabulary semantic segmentation assigns pixels to natural-language concepts while keeping the vision-language backbone frozen. Let the input image be $\mathbf{I} \in \mathbb{R}^{H \times W \times 3}$. A ViT vision encoder partitions \mathbf{I} into non-overlapping patches of size $P \times P$, yielding a grid of $H_p \times W_p$ patches with $H_p = H/P$ and $W_p = W/P$. Denote by $\mathbf{X} \in \mathbb{R}^{N \times D}$ the token matrix at the last Transformer block, with $N = 1 + H_p W_p$ including the CLS token, and write $D = Jd$ for J heads of width d .

After layer normalization, the final block applies multi-head self-attention. For head $j \in \{1, \dots, J\}$, linear projections produce $\mathbf{Q}^{(j)}, \mathbf{K}^{(j)}, \mathbf{V}^{(j)} \in \mathbb{R}^{N \times d}$, and attention is computed as follows:

$$\begin{aligned} \mathbf{A}^{(j)} &= \text{softmax}(d^{-1/2} \mathbf{Q}^{(j)} (\mathbf{K}^{(j)})^\top), \\ \mathbf{Y}^{(j)} &= \mathbf{A}^{(j)} \mathbf{V}^{(j)}. \end{aligned} \quad (1)$$

The head outputs are concatenated and projected, $\mathbf{X}^* = \text{Concat}(\mathbf{Y}^{(1)}, \dots, \mathbf{Y}^{(J)}) \mathbf{W}^o \in \mathbb{R}^{N \times D}$, and the $H_p W_p$ patch rows of \mathbf{X}^* are taken as per-patch features $\mathbf{v}[h, w] \in \mathbb{R}^D$ on the grid $(h, w) \in \{1, \dots, H_p\} \times \{1, \dots, W_p\}$.

Text Encoder. A frozen text encoder maps the label set $\mathcal{Y} = \{y_c\}_{c=1}^C$ to unit-norm prototypes $\mathbf{t}_c \in \mathbb{R}^D$, stacked as $\mathbf{T} = [\mathbf{t}_1^\top; \dots; \mathbf{t}_C^\top] \in \mathbb{R}^{C \times D}$. Patch-text matching then forms initial per-class logits on the patch grid by cosine-scaled similarity $\mathbf{Z} \in \mathbb{R}^{H_p \times W_p \times C}$:

$$\mathbf{Z}[h, w, c] = \alpha \frac{\mathbf{v}[h, w] \cdot \mathbf{t}_c}{\|\mathbf{v}[h, w]\|_2 \|\mathbf{t}_c\|_2}, \quad \alpha = D^{-1/2}. \quad (2)$$

When computed in a single pass, \mathbf{Z} is bilinearly upsampled to image resolution, yielding $\hat{\mathbf{Z}} \in \mathbb{R}^{H \times W \times C}$.

Inference Stage. For high-resolution inputs, the image \mathbf{I} is covered by M overlapping windows $\{\mathbf{I}_m\}_{m=1}^M$. Each window is processed as in Eqs. (1) and (2) to obtain its upsampled logits $\hat{\mathbf{Z}}^{(m)} \in \mathbb{R}^{H \times W \times C}$ in the image coordinate frame. The full-image logits are obtained by weighted fusion on overlaps and are represented as:

$$\hat{\mathbf{Z}}[h, w, c] = \sum_{m=1}^M \omega_m(h, w) \hat{\mathbf{Z}}^{(m)}[h, w, c], \quad (3)$$

where $\sum_{m=1}^M \omega_m(h, w) = 1$, and $\omega_m(h, w)$ are averaging or application-specific weights that vanish outside window m . The zero-shot segmentation map is then given by:

$$\mathbf{S}(\mathbf{I}, \mathcal{Y})[h, w] = \arg \max_{c \in \{1, \dots, C\}} \hat{\mathbf{Z}}[h, w, c]. \quad (4)$$

Eqs. (1)-(4) describe a single, continuous pipeline: the last self-attention block generates patch features, language prototypes provide the semantic anchor, patch-text similarities define class scores, and pixel labels are followed by selection. This baseline presumes a compatible geometry between vision tokens and text prototypes at the patch level. In practice, the contrastive pretraining that prioritizes global alignment of the CLS token often leaves patch interactions noisy and spatially inconsistent. The following sections operate exactly at these two points of fragility: the attention computation in Eq. (1) and the score field in Eq. (2).

3.2. Procrustes Alignment in Self-Attention

Patch-text scores in Eq. (2) assume that the patch features $\mathbf{v}[h, w]$ live in a geometry compatible with the text prototypes. Contrastive pretraining emphasizes global image-text alignment and the last self-attention in Eq. (1) can be dominated by a few background directions, which weakens local correspondence. Before forming scores inside the last block, align the key space to the query space by a single orthogonal map computed per head and per input, as shown in Fig. 2. This preserves norms and angles while correcting the basis mismatch that creates unstable similarities.

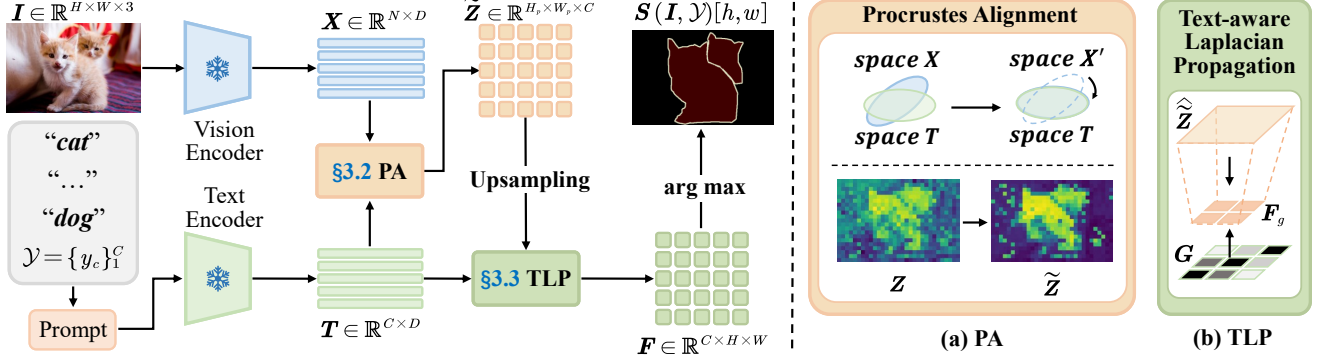


Figure 2. **Our PEARL framework with align-then-propagate.** Given an image I and a label set \mathcal{Y} , a frozen ViT vision encoder yields patch tokens. *Procrustes alignment* is inserted in the last self-attention block: for each head (J heads), queries and keys are weighted-centered and the keys are orthogonally rotated toward the query subspace, producing geometry-corrected patch features. A frozen text encoder maps \mathcal{Y} to unit-norm prototypes T . Patch-text cosine similarity gives initial logits \tilde{Z} . *Text-aware Laplacian propagation* then refines \tilde{Z} on a compact grid using a class graph G induced by T and confidence weights, and the refined scores are upsampled to full resolution F . The final segmentation S is obtained by selecting, at each pixel, the class with the highest score.

Consider one head j (index omitted in matrices for clarity) with queries, keys, and values $Q, K, V \in \mathbb{R}^{N \times d}$ taken from the last block (please refer to §3.1). Tokens are first re-centered to remove global bias. Define nonnegative token weights $\pi_n \propto \|q_n\|_2$ with $\sum_{n=1}^N \pi_n = 1$ and optionally set the CLS weight to zero. With $\mathbf{1} \in \mathbb{R}^{N \times 1}$, the weighted centroids and centered clouds are computed as follows:

$$\begin{aligned} \mu_Q &= \sum_{n=1}^N \pi_n q_n, & \mu_K &= \sum_{n=1}^N \pi_n k_n, \\ Q_c &= Q - \mathbf{1} \mu_Q^\top, & K_c &= K - \mathbf{1} \mu_K^\top. \end{aligned} \quad (5)$$

An orthogonal Procrustes problem aligns keys to queries:

$$R^* = \arg \min_{R \in O(d)} \|K_c R - Q_c\|_F^2 \iff R^* = UV^\top, \quad (6)$$

where $K_c^\top Q_c = U \Sigma V^\top$. The optimizer is the orthogonal factor of the cross-covariance. It can also be obtained by a few Newton-Schulz iterations on the polar factor for an SVD-free implementation. Only keys are rotated and attention is recomputed within the same block:

$$\begin{aligned} \tilde{K} &= K R^*, \\ \tilde{A} &= \text{softmax}(d^{-1/2} Q \tilde{K}^\top), \\ \tilde{Y} &= \tilde{A} V. \end{aligned} \quad (7)$$

Across heads, $\{\tilde{Y}^{(j)}\}_{j=1}^J$ are concatenated and projected as in §3.1 to yield $\tilde{X}^* \in \mathbb{R}^{N \times D}$. The $H_p W_p$ patch rows of \tilde{X}^* replace $v[h, w]$ in Eq. (2), yielding Procrustes-aligned patch-text logits given by:

$$\tilde{Z}[h, w, c] = \alpha \frac{\tilde{v}[h, w] \cdot t_c}{\|\tilde{v}[h, w]\|_2 \|t_c\|_2}, \quad \alpha = D^{-1/2}. \quad (8)$$

This step acts where attention scores are formed. Weighted centering in Eq. (5) dampens the influence of

high-norm background tokens and the CLS summary, while the orthogonal map in Eq. (6) rotates the key basis toward the query basis without changing local magnitudes. The result is a set of patch features whose inner products better reflect directional agreement in the query subspace, which stabilizes the downstream cosine similarities. The extra cost per head is a compact $d \times d$ SVD and two $N \times d$ multiplications, comparable to the baseline attention.

3.3. Text-aware Laplacian Propagation

Even with improved geometry, the score field can remain locally noisy in regions with weak evidence or fine structures. A single refinement pass converts these scores into coherent masks by coupling image boundaries with relations induced by the text prototypes. Language serves not only as a classifier but also as a structural prior that governs how labels propagate across neighboring patches.

Let $\tilde{Z} \in \mathbb{R}^{H \times W \times C}$ be the upsampled logits from Eq. (8). They are averaged on a small grid of size $H_g \times W_g$ (adaptive pooling), giving $Z_g \in \mathbb{R}^{C \times H_g \times W_g}$. On each grid node i of a 4-connected graph $\mathcal{G} = (\mathcal{V}, \mathcal{E})$, set $p_i = \text{softmax}(Z_{g,i}) \in \mathbb{R}^C$. Text prototypes define a class similarity that encodes semantic proximity:

$$G = \text{row-softmax}(T T^\top / \tau_s) + \beta \mathbb{I}_C, \quad (9)$$

where row-softmax applies a softmax independently to each row, $\tau_s > 0$ is a temperature, and \mathbb{I}_C is the $C \times C$ identity. After adding the diagonal term, we re-normalize rows to sum to 1. Confidence at node i combines peak probability with agreement to the text prior:

$$\begin{aligned} \gamma_i &= \max_c p_i(c), & u_i &= p_i^\top G p_i, \\ \rho_i &= (\max\{\gamma_i, \epsilon\})^2 (1 + u_i), \end{aligned} \quad (10)$$

Table 1. **Quantitative results of open-vocabulary semantic segmentation.** “Extra data” denotes external datasets (e.g., CC3M [55], CC12M [11], RedCaps [20], COCO Captions [14, 40], and ImageNet-1K [19]), and “Extra backbone” lists auxiliary models. “Training-free” indicates no extra training. All metrics are mIoU (%). Best results are highlighted with **bold**, and second best with underlined.

Method	Pub. & Year	Extra data	Extra backbone	Training free	with background			without background			Avg.		
					V21	PC60	Object	V20	PC59	Stuff		City	ADE
(a) Trained + Extra data													
GroupViT [69]	CVPR’22	CC12M+RedCaps	✗	✗	50.4	18.7	27.5	79.7	23.4	15.3	11.1	9.2	29.4
TCL [10]	CVPR’23	CC3M+CC12M	✗	✗	51.2	24.3	30.4	77.5	30.3	19.6	23.1	14.9	33.9
CoDe [64]	CVPR’24	CC3M+RedCaps	✗	✗	57.7	30.5	32.3	-	-	23.9	28.9	17.7	-
Trained + Extra data & backbone													
SAM-CLIP [63]	CVPR’24	Merged-41M	SAMv1 (ViT-B/16)	✗	60.6	29.2	-	-	-	31.5	-	17.1	-
CLIP-DINOiser [66]	ECCV’24	ImageNet-1K	DINOv1 (ViT-B/16)	✗	62.1	32.4	34.8	80.9	35.9	24.6	31.7	<u>20.0</u>	40.3
(b) Training-free + Extra data													
ReCo [57]	NeurIPS’22	ImageNet-1K	✗	✓	25.1	19.9	15.7	57.7	22.3	14.8	21.6	11.2	23.5
FOSSIL [3]	WACV’24	COCO Captions	✗	✓	-	-	-	-	35.8	24.8	23.2	18.8	-
Training-free + Extra data & backbone													
FreeDA [4]	CVPR’24	COCO Captions	DINOv2 (ViT-B/14)	✓	51.7	32.6	24.4	77.1	37.1	24.9	34.0	19.5	37.7
(c) Training-free + Extra backbone													
PhP-OVSS [43]	CVPR’24	✗	BLIP (ViT-L/16)	✓	-	-	36.2	51.3	28.0	17.9	-	14.2	-
LaVG [30]	ECCV’24	✗	DINOv1 (ViT-B/8)	✓	62.1	31.6	34.2	82.5	34.7	23.2	26.2	15.8	38.8
ProxyCLIP* [35]	ECCV’24	✗	DINOv2 [†] (ViT-B/14)	✓	58.6	33.8	<u>37.4</u>	83.0	37.2	25.4	33.9	19.7	41.1
LPOSS* [59]	CVPR’25	✗	DINOv1 (ViT-B/16)	✓	61.1	<u>34.6</u>	33.4	78.8	<u>37.8</u>	25.9	<u>37.3</u>	21.8	41.3
CASS* [32]	CVPR’25	✗	DINOv2 [†] (ViT-B/14)	✓	58.6	32.1	33.1	86.1	35.3	23.9	34.1	17.6	40.1
CASS* [32]	CVPR’25	✗	DINOv3 (ViT-B/16)	✓	<u>62.3</u>	34.0	36.0	87.6	37.6	25.4	36.2	18.8	<u>42.2</u>
(d) Training-free + No extra data & backbone													
CLIP [51]	ICML’21	✗	✗	✓	18.6	7.8	6.5	49.1	11.2	7.2	6.7	3.2	13.8
MaskCLIP [81]	ECCV’22	✗	✗	✓	38.3	23.6	20.6	74.9	26.4	16.4	12.6	9.8	27.9
GEM [6]	CVPR’24	✗	✗	✓	46.2	-	-	-	32.6	15.7	-	-	-
CaR [60]	CVPR’24	✗	✗	✓	48.6	13.6	15.4	73.7	18.4	-	-	5.4	-
CLIPtrase [54]	ECCV’24	✗	✗	✓	50.9	29.9	43.6	81.0	33.8	22.8	21.3	16.4	32.7
ClearCLIP [36]	ECCV’24	✗	✗	✓	51.8	32.6	33.0	80.9	35.9	23.9	30.0	16.7	38.1
SCLIP* [62]	ECCV’24	✗	✗	✓	59.1	30.4	30.5	80.4	34.1	22.4	32.2	16.1	38.2
NACLIP* [26]	WACV’25	✗	✗	✓	58.9	32.2	33.2	79.7	35.2	23.3	35.5	17.4	39.4
SFP* [28]	ICCV’25	✗	✗	✓	56.8	32.3	32.1	83.4	36.0	24.0	34.1	18.1	39.6
PEARL (Ours)		✗	✗	✓	64.1	35.1	37.3	<u>86.9</u>	38.6	<u>26.3</u>	37.6	19.4	43.2

Notes: “*” denotes performance reproduced in this work. “†” indicates DINOv2 with registers [18]. Dashes (-) denote numbers not reported.

where $\epsilon > 0$ avoids vanishing weights. Neighboring nodes $(i, j) \in \mathcal{E}$ receive an image edge strength and a text-consistency gate, which are formulated as follows:

$$\begin{aligned}
 b_{ij}^{\text{img}} &= \exp(-\kappa \|\nabla \mathbf{I}\|_{ij}), \\
 g_{ij} &= \text{clip}_{[0,1]}(\mathbf{p}_i^\top \mathbf{G} \mathbf{p}_j), \\
 a_{ij} &= b_{ij}^{\text{img}}(1 + \lambda g_{ij}),
 \end{aligned} \tag{11}$$

with $\kappa > 0$ and $\lambda \geq 0$. Here $\|\nabla \mathbf{I}\|_{ij} := |\tilde{I}_i - \tilde{I}_j|$ denotes the grayscale difference on edge (i, j) , and $\tilde{I} = \text{Gray}(\mathbf{I})$. Let \mathbf{L} be the weighted graph Laplacian of \mathcal{G} , defined by the weights $\{a_{ij}\}$. Refined logits on the grid minimize a convex quadratic that balances data trust and smoothness along image- and text-consistent edges, which is given by:

$$\begin{aligned}
 \mathcal{L}(\mathbf{F}_g) &= \frac{1}{2} \sum_{i \in \mathcal{V}} \rho_i \|\mathbf{F}_{g,i} - \mathbf{Z}_{g,i}\|_2^2 \\
 &+ \frac{\tau}{2} \sum_{(i,j) \in \mathcal{E}} a_{ij} \|\mathbf{F}_{g,i} - \mathbf{F}_{g,j}\|_2^2, \quad \tau > 0.
 \end{aligned} \tag{12}$$

The resulting normal equations are:

$$(\mathbf{D}_\rho + \tau \mathbf{L}) \mathbf{F}_g = \mathbf{D}_\rho \mathbf{Z}_g, \quad \mathbf{D}_\rho = \text{diag}(\{\rho_i\}), \tag{13}$$

which are symmetric positive definite when at least one $\rho_i > 0$. A small, fixed number of conjugate-gradient iterations suffices on the downsampled grid. The solution is then bilinearly upsampled to $\mathbf{F} \in \mathbb{R}^{C \times H \times W}$ and the final segmentation is obtained by:

$$\mathbf{S}(\mathbf{I}, \mathcal{Y})[h, w] = \arg \max_{c \in \{1, \dots, C\}} \mathbf{F}[c, h, w]. \tag{14}$$

This construction turns language into structure: (i) Eq. (9) captures which classes tend to co-occur or be visually close in the text space, (ii) Eq. (10) enhances the influence of reliable nodes that agree with that prior, and (iii) Eq. (11) permits propagation mostly along boundaries that are weak in the image and strong in the text sense. Combined with the alignment in §3.2, the pipeline first fixes the geometry that produces the scores and then performs one principled propagation step, achieving coherent masks without training and with modest computational overhead.

Table 2. **Quantitative results of open-vocabulary semantic segmentation using average pixel accuracy (pAcc, %)**. Rows are grouped by whether an *extra vision backbone* is used. Best results are highlighted with **bold**, and second best with underlined.

Method	Pub. & Year	Extra backbone	with background			without background					Avg.
			V21	PC60	Object	V20	PC59	Stuff	City	ADE	
Training-free with extra backbone											
LaVG [30]	ECCV'24	DINOv1 (ViT-B/8)	89.3	48.7	74.8	91.1	58.9	39.1	68.5	37.0	63.4
ProxyCLIP* [35]	ECCV'24	DINOv2 [†] (ViT-B/14)	86.6	52.0	75.9	88.4	63.4	43.4	<u>74.9</u>	49.1	66.7
CASS* [32]	CVPR'25	DINOv2 [†] (ViT-B/14)	85.6	50.9	70.9	92.2	60.1	41.1	72.5	41.0	64.3
CASS* [32]	CVPR'25	DINOv3 (ViT-B/16)	88.1	53.6	75.5	93.8	62.3	42.0	75.2	45.6	<u>67.0</u>
Training-free without extra backbone											
CLIPtrase [54]	ECCV'24	×	78.6	52.1	50.1	89.7	58.9	38.9	63.4	38.6	59.1
SCLIP* [62]	ECCV'24	×	87.6	49.2	74.3	91.0	58.3	38.4	72.7	38.7	63.8
NACLIP* [26]	WACV'25	×	87.1	51.2	75.3	89.2	59.8	39.3	71.7	45.2	64.9
SFP* [28]	ICCV'25	×	85.3	53.6	71.3	91.9	60.7	41.3	71.7	43.8	65.0
PEARL (Ours)	–	×	<u>88.5</u>	<u>53.5</u>	<u>75.8</u>	<u>93.3</u>	<u>62.9</u>	<u>42.9</u>	73.8	<u>46.9</u>	67.2

Notes: “*” denotes performance reproduced in this work. “†” indicates DINOv2 with registers [18].

4. Experiments

4.1. Experimental Setup

Datasets. Evaluation follows the training-free OVSS protocol on eight widely-used standard benchmarks covering settings *with* and *without* an explicit background class. The *with background* group comprises Pascal VOC 21 (V21) with 21 categories [23], Pascal Context 60 (PC60) with 60 categories [44], and COCO-Object (Object) with 80 object categories derived from MS-COCO [40]. The *without background* group comprises Pascal VOC 20 (V20) with 20 categories [23], Pascal Context 59 (PC59) with 59 categories [44], COCO-Stuff (Stuff) with 171 classes [8], Cityscapes (City) with 19 classes [17], and ADE20K (ADE) with 150 classes [79]. All results are reported on the official validation splits, using the public class-name lists and the standard ImageNet prompt templates [51] (e.g., “a photo of a class”) without dataset-specific prompt engineering, in line with common practice [26, 28, 62].

Implementation Details. PEARL is applied strictly at test time on a frozen vision-language backbone. Unless otherwise stated, we use **CLIP ViT-B/16** for both the vision and text encoders [51]. Two modular components are enabled: (i) *Procrustes alignment* in the last self-attention block, which computes a per-head, per-image orthogonal map to align keys to queries, and (ii) *text-aware Laplacian propagation*, which refines the class-logit map on a compact grid by solving a small symmetric positive-definite linear system with a fixed number of conjugate-gradient iterations before the final upsampling. By default, the grid size in §3.3 is set by (H_g, W_g) . we use $(H_g, W_g) = (224, 224)$ for City, and $(80, 80)$ otherwise. The larger grid on City prevents oversmoothing of thin structures and fine-grained “stuff” detail in high-resolution scenes. No auxiliary backbones, additional training, or external supervision are used. Additional experimental details, including model hyperparameter settings, are provided in the appendix.

Evaluation Protocol and Metric. Following the prior training-free OVSS protocol [26, 28, 36, 54, 62], input images are resized to have a shorter side of 336 pixels (City uses 560 due to its higher base resolution). We adopt sliding-window inference with a 224×224 crop and stride 112, following previous works [26, 28, 62]. All results are single-scale (no multi-scale, no flips). For fair comparison, *no* DenseCRF [34] or PAMR [1] refinement is used in any reported number. Performance is measured primarily with mean Intersection-over-Union (**mIoU**), complemented by pixel accuracy (**pAcc**) for a broader assessment. All experiments are run on a single NVIDIA V100 (32 GB).

4.2. Comparison with SOTA Methods

Quantitative Results (mIoU). Table 1 presents a comprehensive comparison under the training-free OVSS protocol. Among methods that *do not* use auxiliary vision backbones, our method, PEARL, delivers the best average mIoU of **43.2**, clearly surpassing recent strong baselines such as NA-CLIP [26] (39.4) and SFP [28] (39.6). PEARL ranks first on V21 [23] (**64.1**), PC59 [44] (**38.6**), and City [17] (**37.6**), and remains competitive on V20 [23] (**86.9**), where the very best result (87.6) comes from a system that *does* rely on a DINOv3 backbone [58]. Compared with training-free approaches that *do* add powerful backbones, PEARL is within striking distance of the best averages (e.g., CASS [32] with DINOv3 [58] at 42.2), despite using a single frozen CLIP encoder. Two exceptions are worth noting: on Object [40] and ADE [79], PEARL trails the very best numbers by a small margin. For Object [40] (only “things” classes), methods that explicitly model background cleaning or leverage DINO-style objectness have a slight advantage. PEARL does not use any background-cleaning heuristic. For ADE [79], the fine-grained, diverse taxonomy dilutes text-vision agreement at the patch level. we find that generic CLIP prompts sometimes under-specify rare “stuff” categories, which limits zero-shot matching.

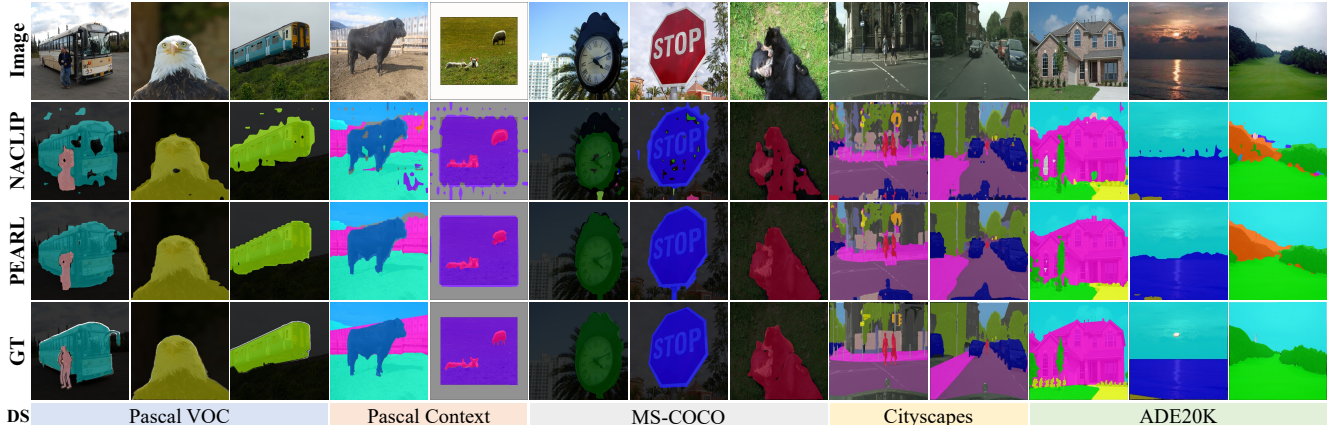


Figure 3. **Qualitative results of open-vocabulary semantic segmentation.** Results are shown on the Pascal VOC [23], Pascal Context [44], MS-COCO [40], Cityscapes [54], and ADE20K [79] datasets (DS), comparing PEARL (ours) with NACLIP [26] and SFP [28]. All methods use CLIP ViT-B/16 [51], and no post-processing (e.g., PAMR [1] or DenseCRF [34]) is applied for a fair comparison.

Quantitative Results (pAcc). Table 2 reports pixel accuracy and compares state-of-the-art training-free OVSS methods. PEARL achieves the best training-free no extra backbone average of **67.2**, and is consistently first or second across datasets, especially on V20 [23], PC59 [44], and City [17], indicating that Procrustes alignment stabilizes token geometry for “things”, while the text-aware Laplacian propagation improves coherence in “stuff” without post-processing. Where we lag slightly (PC60: 53.5 vs. SFP [28] 53.6, ADE: 46.9 vs. ProxyCLIP [35] 49.1), the gap stems from the absence of auxiliary DINO-like region grouping, which particularly benefits fine-grained, diverse “stuff” layouts (i.e., ADE [79]) and the broader class set in PC60 [44]. PEARL outperforms the top average pAcc (CASS [32]+DINOv3 [58] at 67.0) by **0.2**, while remaining strictly training-free and using no extra backbone.

Qualitative Results. As shown in Fig. 3, we compare NACLIP [26] and PEARL across scenes from Pascal VOC/Context [23, 44], MS-COCO [40], Cityscapes [17], and ADE20K [79]. In this work, our PEARL consistently removes spurious “islands” and fills missing parts on foreground objects (e.g., vehicles, animals, people). Interiors are smoother and contain fewer holes than with NA-CLIP [26]. Boundaries on large “stuff” (road, sky, water, facades) are also cleaner, especially around thin structures such as poles and signs. These effects reflect the Procrustes alignment, which sharpens token geometry, followed by a single text-aware Laplacian propagation that performs class-conditioned smoothing. A recurring failure appears in the last ADE20K [79] column. This confusion is common in training-free OVSS [5, 22, 29, 35, 74]. Distant “trees” often form coarse, low-frequency textures that resemble “mountain” patterns, and CLIP [51] text prototypes place semantically related classes close in embedding space. Without task-specific training, richer multi-prompt context, or auxiliary depth/shape cues, the decision can skew toward the more generic terrain label.

Table 3. **Ablation analysis of key components, i.e., PA (cf. §3.2) and TLP (cf. §3.3).** “BG” means the background class.

Component	with BG			without BG			Avg.			
	PA	TLP	Avg.	V21	PC60	Object		V20	PC59	Stuff
✗	✗	18.6	7.8	6.5	49.1	11.2	7.2	6.7	3.2	13.8
✓	✗	59.2	33.0	34.3	85.0	35.3	24.5	35.0	17.9	40.6
✗	✓	35.4	22.4	23.4	79.3	25.0	16.9	20.5	11.7	29.3
✓	✓	64.1	35.1	37.3	86.9	38.6	26.3	37.6	19.4	43.2

Table 4. **Ablation analysis of plug-and-play TLP (cf. §3.3).**

Method	with BG			without BG			Avg.		
	V21	PC60	Object	V20	PC59	Stuff		City	ADE
SCLIP [62]	59.1	30.4	30.5	80.4	34.1	22.4	32.2	16.1	38.2
+ TLP	63.4	34.5	36.2	85.7	37.5	25.7	35.9	18.7	42.2
NACLIP [26]	58.9	32.2	33.2	79.7	35.2	23.3	35.5	17.4	39.4
+ TLP	63.3	34.7	36.2	83.9	38.1	25.7	37.9	18.9	42.3
SFP [28]	56.8	32.3	32.1	83.4	36.0	24.0	34.1	18.1	39.6
+ TLP	58.8	34.1	35.0	85.3	38.1	25.8	35.8	19.4	41.5

4.3. Ablation Studies

We ablate the main components of PEARL, i.e., Procrustes Alignment (PA) and Text-aware Laplacian Propagation (TLP), along with its design and efficiency, reporting all results in mIoU. See the appendix for more details.

Effect of PA and TLP. From Table 3, vanilla CLIP [51] is the baseline with both modules off. Enabling PA alone raises the average from 13.8 to **40.6** by fixing the place where attention is formed. PA rotates keys toward queries inside the last attention block so that patch features and text prototypes compare in a better coordinate system. Turning on TLP alone improves the average to **29.3** by turning noisy scores into smoother and more coherent masks. TLP links pixels that agree in the text space and keeps boundaries where image edges are strong. Activating both delivers the best average of **43.2** with consistent gains with and without

Table 5. Ablation analysis of using different input image sizes.

Size	with BG			without BG				Avg.	
	V21	PC60	Object	V20	PC59	Stuff	City		ADE
224px	59.1	33.1	36.1	86.1	36.4	24.9	29.5	17.7	40.4
280px	61.1	34.4	37.4	86.8	37.8	26.0	32.6	19.2	41.9
336px	64.1	35.1	37.3	86.9	38.6	26.3	33.9	19.4	42.7

Table 6. Ablation analysis of using different CLIP backbones.

Method	CLIP	with BG		without BG		Avg.
		V21	PC59	Stuff	ADE	
SCLIP [62]	ViT-B/32	50.6	28.7	20.0	14.8	28.5
NACLIP [26]		51.1	32.4	21.2	14.9	29.9
SFP* [28]		50.1	31.9	21.3	15.7	29.8
PEARL		54.5	34.7	23.3	16.6	32.3
SCLIP [62]	ViT-L/14	44.4	25.2	17.6	10.9	24.5
NACLIP [26]		52.2	32.1	21.4	17.3	30.8
SFP* [28]		43.8	30.4	20.8	17.0	28.0
PEARL		56.6	36.3	24.8	20.7	34.6

Notes: “*” denotes performance reproduced in this work.

background. Typical improvements include V21 (59.2 → **64.1**), PC59 (35.3 → **38.6**), and City (35.0 → **37.6**).

TLP on Existing Training-Free Methods. Table 4 reports the effect of adding plug-and-play TLP to previous methods without changing backbones or prompts. TLP lifts SCLIP [62] from 38.2 to **42.2**, NACLIP [26] from 39.4 to **42.3**, and SFP [28] from 39.6 to **41.5**. Gains are larger on PC59, Stuff, and City, where class-conditioned propagation helps large regions while preserving thin structures.

Input Resolution. Table 5 shows the results when inputs are resized to short sides of 224, 280, and 336 pixels for *all* datasets, including City [17]. The average increases from 40.4 at 224px to 41.9 at 280px and to **42.7** at 336px. City improves from 29.5 → 32.6 → **33.9**, and ADE from 17.7 → 19.2 → **19.4**. Higher resolution gives more stable patch tokens for PA and clearer local edges for TLP. We adopt 336px by default for a good accuracy-efficiency trade-off and to match prior training-free settings for fair comparison.

Impact of CLIP Backbone. As summarized in Table 6, we present the ablation results for different CLIP backbones, *i.e.*, ViT-B/32 and ViT-L/14. PEARL is strongest within each group with averages of **32.3** (B/32) and **34.6** (L/14). On ADE, PEARL using ViT-L/14 reaches **20.7**, which is higher than our ViT-B/16 result reported elsewhere. ADE contains many fine-grained “*stuff*” regions and diverse scene layouts, and the longer context of L/14 helps TLP connect semantically related areas, while PA maintains the geometry stability. On other datasets, the larger model tends to mix tokens more strongly and weakens local contrast at the patch level, thereby reducing the benefit of PA and making it harder to preserve boundaries. Across all benchmarks, ViT-B/16 remains the most reliable overall choice, as it effectively balances locality and global seman-

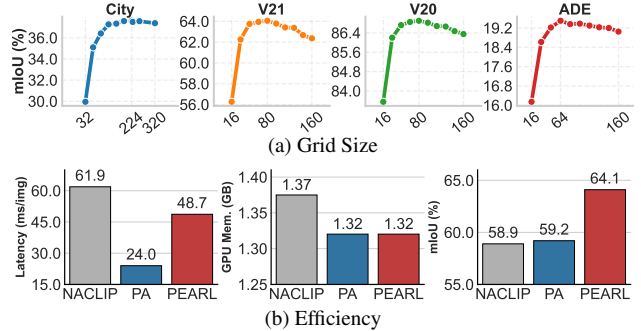


Figure 4. Ablation analysis of (a) grid size and (b) efficiency.

tics. At the same time, ViT-L/14 can be preferable on scenes dominated by broad “*stuff*” regions such as ADE.

Grid Size & Efficiency. Fig. 4a shows mIoU vs. grid size: City peaks at 224, V21/V20 about 80, and ADE at 64. Both overly coarse and fine grids hurt accuracy or efficiency, so we set **224** for City and **80** for all other datasets to achieve a fair and simple setup. As shown in Fig. 4b, on V21 under this setting, PA already surpasses NACLIP, and adding TLP (PEARL) further improves mIoU to **64.1**, while reducing memory from 1.37 to 1.32 GB and latency from 61.9 to 48.7 ms/img, yielding the best accuracy-efficiency trade-off.

5. Conclusion

We present PEARL, a training-free framework for open-vocabulary semantic segmentation that follows an *align-then-propagate* recipe on a frozen vision-language backbone. The first step applies an orthogonal Procrustes alignment within the last self-attention block to align keys with the query subspace after weighted centering, thereby stabilizing token geometry for patch-text matching. The second step performs text-aware Laplacian propagation on a compact grid, where text prototypes provide both a confidence cue and a gate on neighbor links while image edges guide boundaries. Both methods are closed-form, parameter-free, and inexpensive, making the pipeline plug-and-play with CLIP-style inference. Across standard OVSS benchmarks, PEARL consistently improves coherence on small objects and preserves large “*stuff*” regions under a unified evaluation protocol, without auxiliary backbones or training.

Limitation and Future Work. Performance depends on prompt quality and label names, very low-contrast boundaries remain challenging, the grid size trades detail for cost, and the method is not instance-aware. These are common constraints in training-free OVSS and motivate future work on prompt calibration, adaptive grids, and instance cues.

Acknowledgement. This work was supported by the National Natural Science Foundation of China (No. 62472222), Natural Science Foundation of Jiangsu Province (No. BK20240080), and in part by the Institute of Information & communications Technology Planning & Evaluation (IITP) grant funded by the Korea government (MSIT) (No. RS-2024-00337489).

References

- [1] Nikita Araslanov and Stefan Roth. Single-stage semantic segmentation from image labels. In *CVPR*, pages 4253–4262, 2020. 2, 3, 6, 7, 4, 5
- [2] Sule Bai, Yong Liu, Yifei Han, Haoji Zhang, Yansong Tang, Jie Zhou, and Jiwen Lu. Self-calibrated clip for training-free open-vocabulary segmentation. *TIP*, 34:8271–8284, 2025. 3
- [3] Luca Barsellotti, Roberto Amoroso, Lorenzo Baraldi, and Rita Cucchiara. FOSSIL: Free open-vocabulary semantic segmentation through synthetic references retrieval. In *WACV*, pages 1464–1473, 2024. 3, 5
- [4] Luca Barsellotti, Roberto Amoroso, Marcella Cornia, Lorenzo Baraldi, and Rita Cucchiara. Training-free open-vocabulary segmentation with offline diffusion-augmented prototype generation. In *CVPR*, pages 3689–3698, 2024. 3, 5
- [5] Luca Barsellotti, Lorenzo Bianchi, Nicola Messina, Fabio Carrara, Marcella Cornia, Lorenzo Baraldi, Fabrizio Falchi, and Rita Cucchiara. Talking to dino: Bridging self-supervised vision backbones with language for open-vocabulary segmentation. In *ICCV*, pages 22025–22035, 2025. 1, 2, 3, 7
- [6] Walid Boussethem, Felix Petersen, Vittorio Ferrari, and Hilde Kuehne. Grounding everything: Emerging localization properties in vision-language transformers. In *CVPR*, pages 3828–3837, 2024. 2, 3, 5
- [7] Maxime Bucher, Tuan-Hung Vu, Matthieu Cord, and Patrick Perez. Zero-shot semantic segmentation. In *NeurIPS*, pages 469–479, 2019. 1, 2
- [8] Holger Caesar, Jasper Uijlings, and Vittorio Ferrari. COCO-Stuff: Thing and stuff classes in context. In *CVPR*, pages 1209–1218, 2018. 6, 1, 3, 5
- [9] Mathilde Caron, Hugo Touvron, Ishan Misra, Hervé Jégou, Julien Mairal, Piotr Bojanowski, and Armand Joulin. Emerging properties in self-supervised vision transformers. In *ICCV*, pages 9650–9660, 2021. 1, 2, 3
- [10] Junbum Cha, Jonghwan Mun, and Byungseok Roh. Learning to generate text-grounded mask for open-world semantic segmentation from only image-text pairs. In *CVPR*, pages 11165–11174, 2023. 2, 5, 3
- [11] Soravit Changpinyo, Piyush Sharma, Nan Ding, and Radu Soricut. Conceptual 12m: Pushing web-scale image-text pre-training to recognize long-tail visual concepts. In *CVPR*, pages 3558–3568, 2021. 5, 3
- [12] Liang-Chieh Chen, George Papandreou, Iasonas Kokkinos, Kevin Murphy, and Alan L Yuille. Deeplab: Semantic image segmentation with deep convolutional nets, atrous convolution, and fully connected crfs. *TPAMI*, 40(4):834–848, 2017. 2
- [13] Qi Chen, Lingxiao Yang, Yun Chen, Nailong Zhao, Jianhuang Lai, Jie Shao, and Xiaohua Xie. Training-free class purification for open-vocabulary semantic segmentation. In *ICCV*, pages 23124–23134, 2025. 3
- [14] Xinlei Chen, Hao Fang, Tsung-Yi Lin, Ramakrishna Vedantam, Saurabh Gupta, Piotr Dollár, and C Lawrence Zitnick. Microsoft coco captions: Data collection and evaluation server. *arXiv preprint arXiv:1504.00325*, 2015. 5, 3
- [15] Zhixiang Chi, Yanan Wu, Li Gu, Huan Liu, Ziqiang Wang, Yang Zhang, Yang Wang, and Konstantinos Plataniotis. Plug-in feedback self-adaptive attention in clip for training-free open-vocabulary segmentation. In *ICCV*, pages 22815–22825, 2025. 3
- [16] Seokju Cho, Heeseong Shin, Sunghwan Hong, Anurag Arnab, Paul Hongsuck Seo, and Seungryong Kim. CAT-Seg: Cost aggregation for open-vocabulary semantic segmentation. In *CVPR*, pages 4113–4123, 2024. 1, 2
- [17] Marius Cordts, Mohamed Omran, Sebastian Ramos, Timo Rehfeld, Markus Enzweiler, Rodrigo Benenson, Uwe Franke, Stefan Roth, and Bernt Schiele. The cityscapes dataset for semantic urban scene understanding. In *CVPR*, pages 3213–3223, 2016. 2, 6, 7, 8, 1, 3
- [18] Timothee Darcet, Maxime Oquab, Julien Mairal, and Piotr Bojanowski. Vision transformers need registers. In *ICLR*, 2024. 5, 6, 3
- [19] Jia Deng, Wei Dong, Richard Socher, Li-Jia Li, Kai Li, and Li Fei-Fei. Imagenet: A large-scale hierarchical image database. In *CVPR*, pages 248–255, 2009. 5, 3
- [20] Karan Desai, Gaurav Kaul, Zubin Aysola, and Justin Johnson. Redcaps: Web-curated image-text data created by the people, for the people. *arXiv preprint arXiv:2111.11431*, 2021. 5, 3
- [21] Alexey Dosovitskiy, Lucas Beyer, Alexander Kolesnikov, Dirk Weissenborn, Xiaohua Zhai, Thomas Unterthiner, Mostafa Dehghani, Matthias Minderer, Georg Heigold, Sylvain Gelly, Jakob Uszkoreit, and Neil Houlsby. An image is worth 16x16 words: Transformers for image recognition at scale. In *ICLR*, 2021. 1
- [22] Songsong Duan, Xi Yang, and Nannan Wang. Dih-clip: Unleashing the diversity of multi-head self-attention for training-free open-vocabulary semantic segmentation. In *ICCV*, pages 22794–22803, 2025. 3, 7
- [23] Mark Everingham, SM Ali Eslami, Luc Van Gool, Christopher KI Williams, John Winn, and Andrew Zisserman. The pascal visual object classes challenge: A retrospective. *IJCV*, 111(1):98–136, 2015. 2, 6, 7, 1, 3, 4, 5
- [24] Yuxin Fang, Wen Wang, Binhui Xie, Quan Sun, Ledell Wu, Xinggang Wang, Tiejun Huang, Xinlong Wang, and Yue Cao. EVA: Exploring the limits of masked visual representation learning at scale. In *CVPR*, pages 19358–19369, 2023. 2
- [25] Golnaz Ghiasi, Xiuye Gu, Yin Cui, and Tsung-Yi Lin. Scaling open-vocabulary image segmentation with image-level labels. In *ECCV*, pages 540–557, 2022. 2
- [26] Sina Hajimiri, Ismail Ben Ayed, and Jose Dolz. Pay attention to your neighbours: Training-free open-vocabulary semantic segmentation. In *WACV*, pages 5061–5071, 2025. 1, 2, 3, 5, 6, 7, 8
- [27] Chao Jia, Yinfei Yang, Ye Xia, Yi-Ting Chen, Zarana Parekh, Hieu Pham, Quoc Le, Yun-Hsuan Sung, Zhen Li, and Tom Duerig. Scaling up visual and vision-language representation learning with noisy text supervision. In *ICML*, pages 4904–4916, 2021. 1, 2
- [28] Shuo Jin, Siyue Yu, Bingfeng Zhang, Mingjie Sun, Yi Dong, and Jimin Xiao. Feature purification matters: Suppressing

- outlier propagation for training-free open-vocabulary semantic segmentation. In *ICCV*, pages 20291–20300, 2025. [2](#), [3](#), [5](#), [6](#), [7](#), [8](#)
- [29] Cijo Jose, Theo Moutakanni, Dahyun Kang, Federico Baldassarre, Timothee Darcet, Hu Xu, Daniel Li, Marc Szafraniec, Michael Ramamonjisoa, and Maxime Oquab. Dinov2 meets text: A unified framework for image- and pixel-level vision-language alignment. *CVPR*, pages 24905–24916, 2025. [2](#), [3](#), [7](#)
- [30] Dahyun Kang and Minsu Cho. In defense of lazy visual grounding for open-vocabulary semantic segmentation. In *ECCV*, pages 143–164, 2024. [2](#), [5](#), [6](#), [3](#)
- [31] Seil Kang, Jinyeong Kim, Junhyeok Kim, and Seong Jae Hwang. Your large vision-language model only needs a few attention heads for visual grounding. In *CVPR*, pages 9339–9350, 2025. [3](#)
- [32] Chanyoung Kim, Dayun Ju, Woojung Han, Ming-Hsuan Yang, and Seong Jae Hwang. Distilling spectral graph for object-context aware open-vocabulary semantic segmentation. In *CVPR*, pages 15033–15042, 2025. [1](#), [2](#), [5](#), [6](#), [7](#), [3](#)
- [33] Alexander Kirillov, Eric Mintun, Nikhila Ravi, Hanzi Mao, Chloe Rolland, Laura Gustafson, Tete Xiao, Spencer Whitehead, Alexander C Berg, Wan-Yen Lo, et al. Segment anything. In *ICCV*, pages 4015–4026, 2023. [2](#), [3](#)
- [34] Philipp Krähenbühl and Vladlen Koltun. Efficient inference in fully connected CRFs with Gaussian edge potentials. In *NeurIPS*, pages 109–117, 2011. [2](#), [3](#), [6](#), [7](#), [4](#), [5](#)
- [35] Mengcheng Lan, Chaofeng Chen, Yiping Ke, Xinjiang Wang, Litong Feng, and Wayne Zhang. ProxyCLIP: Proxy attention improves CLIP for open-vocabulary segmentation. In *ECCV*, pages 70–88, 2024. [2](#), [3](#), [5](#), [6](#), [7](#)
- [36] Mengcheng Lan, Chaofeng Chen, Yiping Ke, Xinjiang Wang, Litong Feng, and Wayne Zhang. ClearCLIP: Decomposing CLIP representations for dense vision-language inference. In *ECCV*, pages 143–160, 2024. [2](#), [3](#), [5](#), [6](#)
- [37] Boyi Li, Kilian Q. Weinberger, Serge Belongie, Vladlen Koltun, and René Ranftl. Language-driven semantic segmentation. In *ICLR*, 2022. [1](#), [2](#)
- [38] Liunian Harold Li, Pengchuan Zhang, Haotian Zhang, Jianwei Yang, Chunyuan Li, Yiwu Zhong, Lijuan Wang, Lu Yuan, Lei Zhang, and Jenq-Neng Hwang. Grounded language-image pre-training. In *CVPR*, pages 10965–10975, 2022. [2](#)
- [39] Feng Liang, Bichen Wu, Xiaoliang Dai, Kunpeng Li, Yinan Zhao, Hang Zhang, Peizhao Zhang, Peter Vajda, and Diana Marculescu. Open-vocabulary semantic segmentation with mask-adapted CLIP. In *CVPR*, pages 7061–7070, 2023. [1](#), [2](#)
- [40] Tsung-Yi Lin, Michael Maire, Serge Belongie, James Hays, Pietro Perona, Deva Ramanan, Piotr Dollár, and C. Lawrence Zitnick. Microsoft COCO: Common objects in context. In *ECCV*, pages 740–755, 2014. [2](#), [5](#), [6](#), [7](#), [1](#), [3](#), [4](#)
- [41] Ze Liu, Yutong Lin, Yue Cao, Han Hu, Yixuan Wei, Zheng Zhang, Stephen Lin, and Baining Guo. Swin transformer: Hierarchical vision transformer using shifted windows. In *ICCV*, pages 10012–10022, 2021. [1](#)
- [42] Jonathan Long, Evan Shelhamer, and Trevor Darrell. Fully convolutional networks for semantic segmentation. In *CVPR*, pages 3431–3440, 2015. [2](#)
- [43] Jiayun Luo, Siddhesh Khandelwal, Leonid Sigal, and Boyang Li. Emergent open-vocabulary semantic segmentation from off-the-shelf vision-language models. In *CVPR*, pages 4029–4040, 2024. [3](#), [5](#)
- [44] Roozbeh Mottaghi, Xianjie Chen, Xiaobai Liu, Nam-Gyu Cho, Seong-Whan Lee, Sanja Fidler, Raquel Urtasun, and Alan Yuille. The role of context for object detection and semantic segmentation in the wild. In *CVPR*, pages 891–898, 2014. [6](#), [7](#), [1](#), [3](#), [4](#), [5](#)
- [45] Jishnu Mukhoti, Tsung-Yu Lin, Omid Poursaeed, Rui Wang, Ashish Shah, Philip H. S. Torr, and Ser-Nam Lim. Open vocabulary semantic segmentation with patch aligned contrastive learning. In *CVPR*, pages 19413–19423, 2023. [1](#)
- [46] Maxime Oquab, Timothee Darcet, Théo Moutakanni, Huy Vo, Marc Szafraniec, Vasil Khalidov, Pierre Fernandez, Daniel Haziza, Francisco Massa, and Alaaeldin El-Nouby. DINOv2: Learning robust visual features without supervision. *arXiv preprint arXiv:2304.07193*, 2023. [1](#), [2](#)
- [47] Gensheng Pei, Fumin Shen, Yazhou Yao, Tao Chen, Xian-Sheng Hua, and Heng-Tao Shen. Hierarchical graph pattern understanding for zero-shot video object segmentation. *TIP*, 32:5909–5920, 2023. [1](#)
- [48] Gensheng Pei, Yazhou Yao, Fumin Shen, Dan Huang, Xingguo Huang, and Heng-Tao Shen. Hierarchical co-attention propagation network for zero-shot video object segmentation. *TIP*, 32:2348–2359, 2023. [1](#)
- [49] Gensheng Pei, Tao Chen, Yujia Wang, Xinhao Cai, Xiangbo Shu, Tianfei Zhou, and Yazhou Yao. Seeing what matters: Empowering clip with patch generation-to-selection. In *CVPR*, pages 24862–24872, 2025. [2](#)
- [50] Gensheng Pei, Xiruo Jiang, Yazhou Yao, Xiangbo Shu, Fumin Shen, and Byeungwoo Jeon. Taming sam3 in the wild: A concept bank for open-vocabulary segmentation. *arXiv preprint arXiv:2602.06333*, 2026. [3](#)
- [51] Alec Radford, Jong Wook Kim, Chris Hallacy, Aditya Ramesh, Gabriel Goh, Sandhini Agarwal, Girish Sastry, Amanda Askell, Pamela Mishkin, and Jack Clark. Learning transferable visual models from natural language supervision. In *ICML*, pages 8748–8763, 2021. [1](#), [2](#), [5](#), [6](#), [7](#), [4](#)
- [52] Nikhila Ravi, Valentin Gabeur, Yuan-Ting Hu, Ronghang Hu, Chaitanya Ryali, Tengyu Ma, Haitham Khedr, Roman Rädle, Chloe Rolland, Laura Gustafson, Eric Mintun, Junting Pan, Kalyan Vasudev Alwala, Nicolas Carion, Chao-Yuan Wu, Ross Girshick, Piotr Dollar, and Christoph Feichtenhofer. SAM 2: Segment anything in images and videos. In *ICLR*, 2025. [2](#)
- [53] Robin Rombach, Andreas Blattmann, Dominik Lorenz, Patrick Esser, and Björn Ommer. High-resolution image synthesis with latent diffusion models. In *CVPR*, pages 10684–10695, 2022. [3](#)
- [54] Tong Shao, Zhuotao Tian, Hang Zhao, and Jingyong Su. Explore the potential of clip for training-free open vocabulary semantic segmentation. In *ECCV*, pages 139–156, 2024. [2](#), [3](#), [5](#), [6](#), [7](#)

- [55] Piyush Sharma, Nan Ding, Sebastian Goodman, and Radu Soricut. Conceptual captions: A cleaned, hypernymed, image alt-text dataset for automatic image captioning. In *ACL*, pages 2556–2565, 2018. 5, 3
- [56] Yuheng Shi, Minjing Dong, and Chang Xu. Harnessing vision foundation models for high-performance, training-free open vocabulary segmentation. In *ICCV*, pages 23487–23497, 2025. 3
- [57] Gyungin Shin, Weidi Xie, and Samuel Albanie. ReCo: Retrieve and co-segment for zero-shot transfer. In *NeurIPS*, pages 33754–33767, 2022. 5, 3
- [58] Oriane Siméoni, Huy V Vo, Maximilian Seitzer, Federico Baldassarre, Maxime Oquab, Cijo Jose, Vasil Khalidov, Marc Szafraniec, Seungeun Yi, Michaël Ramamonjisoa, et al. Dinov3. *arXiv preprint arXiv:2508.10104*, 2025. 1, 2, 6, 7
- [59] Vladan Stojnić, Yannis Kalantidis, Jiří Matas, and Giorgos Tolias. Lposs: Label propagation over patches and pixels for open-vocabulary semantic segmentation. In *CVPR*, pages 9794–9803, 2025. 2, 5
- [60] Shuyang Sun, Runjia Li, Philip Torr, Xiuye Gu, and Siyang Li. CLIP as RNN: Segment countless visual concepts without training endeavor. In *CVPR*, pages 13171–13182, 2024. 2, 3, 5
- [61] Hugo Touvron, Matthieu Cord, Matthijs Douze, Francisco Massa, Alexandre Sablayrolles, and Hervé Jégou. Training data-efficient image transformers & distillation through attention. In *ICML*, pages 10347–10357, 2021. 1
- [62] Feng Wang, Jieru Mei, and Alan Yuille. SCLIP: Rethinking self-attention for dense vision-language inference. In *ECCV*, pages 315–332, 2024. 5, 6, 7, 8, 3
- [63] Haoxiang Wang, Pavan Kumar Anasosalu Vasu, Fartash Faghri, Raviteja Vemulapalli, Mehrdad Farajtabar, Sachin Mehta, Mohammad Rastegari, Oncel Tuzel, and Hadi Pouransari. Sam-clip: Merging vision foundation models towards semantic and spatial understanding. In *CVPR*, pages 3635–3647, 2024. 3, 5
- [64] Ji-Jia Wu, Andy Chia-Hao Chang, Chieh-Yu Chuang, Chun-Pei Chen, Yu-Lun Liu, Min-Hung Chen, Hou-Ning Hu, Yung-Yu Chuang, and Yen-Yu Lin. Image-text co-decomposition for text-supervised semantic segmentation. In *CVPR*, pages 26794–26803, 2024. 5
- [65] Monika Wysoczanska, Michaël Ramamonjisoa, Tomasz Trzcinski, and Oriane Siméoni. CLIP-DIY: CLIP dense inference yields open-vocabulary semantic segmentation for free. In *WACV*, pages 1403–1413, 2024. 2, 3
- [66] Monika Wysoczanska, Oriane Simeoni, Michaël Ramamonjisoa, Andrei Bursuc, Tomasz Trzcinski, and Patrick Perez. CLIP-DINOiser: Teaching CLIP a few DINO tricks for open-vocabulary semantic segmentation. In *ECCV*, pages 320–337, 2024. 2, 3, 5
- [67] Bin Xie, Jiale Cao, Jin Xie, Fahad Shahbaz Khan, and Yanwei Pang. SED: A simple encoder-decoder for open-vocabulary semantic segmentation. In *CVPR*, pages 3426–3436, 2024. 1, 2
- [68] Enze Xie, Wenhai Wang, Zhiding Yu, Anima Anandkumar, Jose M Alvarez, and Ping Luo. Segformer: Simple and efficient design for semantic segmentation with transformers. In *NeurIPS*, pages 12077–12090, 2021. 2
- [69] Jiarui Xu, Shalini De Mello, Sifei Liu, Wonmin Byeon, Thomas Breuel, Jan Kautz, and Xiaolong Wang. GroupViT: Semantic segmentation emerges from text supervision. In *CVPR*, pages 18134–18144, 2022. 2, 5, 3
- [70] Jilan Xu, Junlin Hou, Yuejie Zhang, Rui Feng, Yi Wang, Yu Qiao, and Weidi Xie. Learning open-vocabulary semantic segmentation models from natural language supervision. In *CVPR*, pages 2935–2944, 2023.
- [71] Jiarui Xu, Sifei Liu, Arash Vahdat, Wonmin Byeon, Xiaolong Wang, and Shalini De Mello. Open-vocabulary panoptic segmentation with text-to-image diffusion models. In *CVPR*, pages 2955–2966, 2023. 2
- [72] Mengde Xu, Zheng Zhang, Fangyun Wei, Yutong Lin, Yue Cao, Han Hu, and Xiang Bai. A simple baseline for open-vocabulary semantic segmentation with pre-trained vision-language model. In *ECCV*, pages 736–753, 2022. 1, 2
- [73] Mengde Xu, Zheng Zhang, Fangyun Wei, Han Hu, and Xiang Bai. Side adapter network for open-vocabulary semantic segmentation. In *CVPR*, pages 2945–2954, 2023. 1, 2
- [74] Xiwei Xuan, Ziquan Deng, and Kwan-Liu Ma. Reme: A data-centric framework for training-free open-vocabulary segmentation. In *ICCV*, pages 20954–20965, 2025. 2, 3, 7
- [75] Yuhang Yang, Jinhong Deng, Wen Li, and Lixin Duan. Resclip: Residual attention for training-free dense vision-language inference. In *CVPR*, pages 29968–29978, 2025. 3
- [76] Dengke Zhang, Fagui Liu, and Quan Tang. Corrclip: Reconstructing patch correlations in clip for open-vocabulary semantic segmentation. In *ICCV*, pages 24677–24687, 2025. 2, 3
- [77] Hang Zhao, Xavier Puig, Bolei Zhou, Sanja Fidler, and Antonio Torralba. Open vocabulary scene parsing. In *ICCV*, pages 2002–2010, 2017. 1, 2
- [78] Yiwu Zhong, Jianwei Yang, Pengchuan Zhang, Chunyuan Li, Noel Codella, Liunian Harold Li, Luowei Zhou, Xiyang Dai, Lu Yuan, and Yin Li. RegionCLIP: Region-based language-image pretraining. In *CVPR*, pages 16793–16803, 2022. 2
- [79] Bolei Zhou, Hang Zhao, Xavier Puig, Sanja Fidler, Adela Barriuso, and Antonio Torralba. Scene parsing through ADE20K dataset. In *CVPR*, pages 633–641, 2017. 2, 6, 7, 1, 3
- [80] Bolei Zhou, Hang Zhao, Xavier Puig, Tete Xiao, Sanja Fidler, Adela Barriuso, and Antonio Torralba. Semantic understanding of scenes through the ADE20K dataset. *IJCV*, 127: 302–321, 2019. 2
- [81] Chong Zhou, Chen Change Loy, and Bo Dai. Extract free dense labels from CLIP. In *ECCV*, pages 350–368, 2022. 1, 2, 3, 5
- [82] Xingyi Zhou, Rohit Girdhar, Armand Joulin, Philipp Krähenbühl, and Ishan Misra. Detecting twenty-thousand classes using image-level supervision. In *ECCV*, pages 350–368, 2022. 2



PEARL: Geometry Aligns Semantics for Training-Free Open-Vocabulary Semantic Segmentation

Supplementary Material

Appendix

This appendix presents further model settings (§A), ablation studies (§B), quantitative (§C), and qualitative results (§D).

A. More Model Settings

Hyperparameter setting. For fair and consistent evaluation, we use a unified hyperparameter configuration for all datasets without dataset-specific tuning. The detailed settings are summarized in Table A7.

Table A7. Fixed hyperparameter setting used for all datasets.

Config	τ_s	β	ϵ	κ	λ	τ
Value	0.5	10	10^{-6}	5	1	1

B. More Ablation Studies

Alignment Objective. We further analyze the behavior of Procrustes Alignment (PA) on V21 [23]. PA is applied only to the *last* self-attention layer, where patch-text logits are formed, and aligns the key basis to the query basis ($\mathbf{K} \rightarrow \mathbf{Q}$) to correct token geometry with minimal disturbance to the original similarity structure. As an orthogonal Procrustes map, \mathbf{R}^* is the minimum-change, inner-product-preserving transformation under an orthogonality constraint, which explains why simpler variants such as centering only, whitening, or global rotation are consistently inferior. As shown in Fig. B5(a), PA makes the centered query/key clouds substantially better aligned in the projected space. Fig. B5(b) shows that the learned rotations have non-trivial yet well-behaved magnitudes across image-head pairs, while Fig. B5(c) indicates a positive correlation between alignment-error reduction and mIoU improvement. The component ablation in Fig. B5(d) further confirms that the full weighted formulation performs best, improving over its unweighted counterpart by 4.1 mIoU. Finally, Fig. B5(e)-(f), together with Tables B8 and B9, show that the iterative *Newton-Schulz* (N-S) solver is stable in practice: it matches SVD in accuracy while being substantially faster, and both the N-S iterations and the conjugate-gradient (CG) iterations exhibit clear performance plateaus, motivating the default settings used in all experiments.

Alignment Solver. Consistent with the trend in Fig. B5(e), Table B8 compares SVD and the N-S iterative solver inside our Procrustes alignment. Both solvers achieve the same

Table B8. Ablation analysis of different alignment solvers (*cf.* §3.2). “N-S” denotes the Newton-Schulz iterative algorithm.

Solver	with BG			without BG			Avg.
	V21	PC60	Object	V20	PC59	Stuff City	
SVD	64.2	35.2	37.2	86.7	38.6	26.3 37.9	19.2 43.2
N-S	64.1	35.1	37.3	86.9	38.6	26.3 37.6	19.4 43.2

Table B9. Inference latency (ms/img) comparison of alignment solvers. “N-S” denotes the Newton-Schulz iterative algorithm.

Latency	with BG			without BG			Avg.
	V21	PC60	Object	V20	PC59	Stuff City	
SVD	60.9	199.7	239.3	59.6	198.8	212.1 975.9	192.3 267.3
N-S	48.7	111.7	149.4	47.1	111.2	120.7 498.5	115.4 150.3

average mIoU (43.2), and the per-dataset differences are within 0.3 points: SVD is slightly better on V21/PC60/City, while N-S is slightly better on Object/V20/ADE, indicating that the choice of solver has a negligible impact on accuracy. In terms of efficiency, Table B9 further shows that N-S consistently yields lower inference latency across all datasets (*e.g.*, 48.7 vs. 60.9 ms/img on V21 and 498.5 vs. 975.9 ms/img on City), reducing the average latency from 267.3 to 150.3 ms/img. This speedup is possible because our Procrustes module only requires the orthogonal factor of the SVD of a small $C \times C$ matrix: this factor coincides with the orthogonal polar factor $\mathbf{M}(\mathbf{M}^\top \mathbf{M})^{-1/2}$, where the inverse square root $(\mathbf{M}^\top \mathbf{M})^{-1/2}$ can be efficiently approximated by the N-S iteration (*cf.* §3.2) using only matrix multiplications on the GPU. Therefore, we adopt the SVD-free N-S variant as our default solver, which preserves accuracy while substantially improving efficiency.

Key-Key Self-Correlation. As shown in Table B10, we evaluate the effect of adding a key-key self-correlation term to our Procrustes Alignment (*cf.* §3.2) and enabling this term (*w/*) improves results on all datasets. In the “with BG” group, it brings gains of +0.9, +0.4, and +0.5 mIoU on V21 [23], PC60 [44], and Object [40], respectively. In the “without BG” group, it yields +0.5, +0.3, +0.2, +3.0, and +0.7 mIoU on V20 [23], PC59 [44], Stuff [8], City [17], and ADE [79]. Overall, the average mIoU increases from 42.4 to 43.2 (+0.8), with no degradation on any dataset and a particularly notable boost on City (+3.0), where long-range dependencies and cluttered scenes are common. In our implementation, Procrustes Alignment first recenters queries and

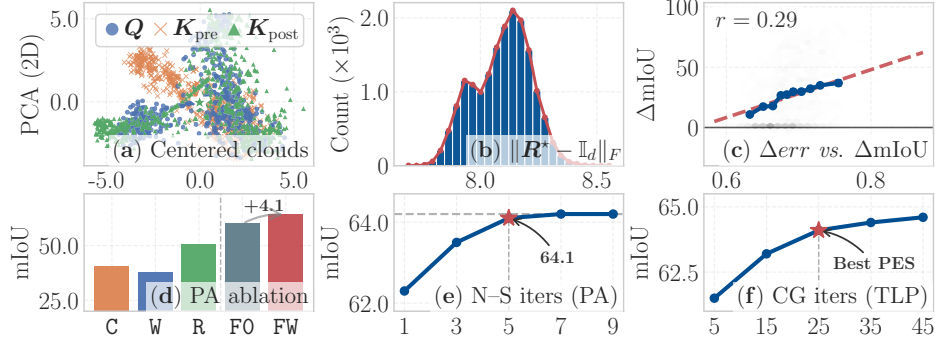


Figure B5. **Diagnostics of Procrustes Alignment on V21 [23].** (a) PCA projection of centered queries and keys before and after PA. (b) Distribution of the per-(image, head) rotation magnitude $\|\mathbf{R}^* - \mathbf{I}_d\|_F$. (c) Correlation between alignment-error reduction Δerr and mIoU gain $\Delta mIoU$. (d) Component ablation of centering (C), whitening (W), rotation (R), full PA without weights (FO), and full weighted PA (FW). (e) Stability of the Newton-Schulz iterations used in PA. (f) Stability of the conjugate-gradient iterations used in TLP.

keys using the token weights π_n in Eq. (5) and solves the orthogonal Procrustes problem in Eq. (6), either via SVD or via an SVD-free Newton-Schulz approximation of the polar factor, to obtain an orthogonal map \mathbf{R}^* that aligns the key basis to the query basis. Aligned attention scores are then computed as in Eq. (7), and we add a lightweight key-key term constructed from the centered keys, $\mathbf{K}_c \mathbf{K}_c^\top$, scaled by a factor $\alpha = d^{-1/2}$. Geometrically, the Procrustes term aligns the cross-covariances ($\mathbf{K}_c^\top \mathbf{Q}_c$) at the first order. Meanwhile, the key-key Gram matrix captures the self-correlation of \mathbf{K}_c , serving as a second-order regularizer for the attention kernel. Since \mathbf{K}_c is already de-biased by weighted centering (which suppresses dominant background and CLS tokens), this self-correlation term reinforces coherent foreground regions while dampening isolated noise. Consequently, the attention mechanism merges query alignment with the internal structure of the key space. This yields more stable token interactions and drives the segmentation improvements shown in Table B10.

Impact of Conjugate-Gradient Iterations. Table B11 and Fig. B5(f) ablate the number of CG iterations used to solve Eq. (13) in our Text-aware Laplacian Propagation (TLP) on V21 [23]. To balance segmentation quality and efficiency, we define a *Precision-Efficiency Score* (PES) that averages normalized mIoU, pAcc, Latency and GPU Memory for each setting. For each metric $q \in \{\text{mIoU}, \text{pAcc}\}$ and $r \in \{\text{Latency}, \text{Memory}\}$, let $q^{\max} = \max_j q_j$, $q^{\min} = \min_j q_j$ and $r^{\max} = \max_j r_j$, $r^{\min} = \min_j r_j$. The normalized scores are represented as follows:

$$q_k^{\text{norm}} = \begin{cases} \frac{q_k - q^{\min}}{q^{\max} - q^{\min}}, & q^{\max} > q^{\min}, \\ 1, & \text{otherwise,} \end{cases} \quad (15)$$

$$r_k^{\text{norm}} = \begin{cases} \frac{r^{\max} - r_k}{r^{\max} - r^{\min}}, & r^{\max} > r^{\min}. \\ 1, & \text{otherwise.} \end{cases} \quad (16)$$

Table B10. **Ablation analysis of a key-key self-correlation term.**

key-key	with BG		without BG				Avg.		
	V21	PC60	Object	V20	PC59	Stuff City		ADE	
w/o	63.2	34.7	36.8	86.4	38.3	26.1	34.6	18.7	42.4
w/	64.1	35.1	37.3	86.9	38.6	26.3	37.6	19.4	43.2

Table B11. **Ablation analysis of CG iterations on V21 [23]** (cf. §3.3. “PES” denotes the precision-efficiency score.

Iteration	Precision		Efficiency		PES
	mIoU	pAcc	Latency (ms/img)	Memory (GB)	
5	61.5	87.4	31.7	1.32	0.50
15	63.2	88.2	40.5	1.32	0.73
25	64.1	88.5	48.7	1.32	0.80
35	64.4	88.7	58.5	1.32	0.79
45	64.6	88.7	66.5	1.32	0.75

Here, mIoU and pAcc are “*the higher the better*”, while Latency and GPU Memory are flipped so that lower cost yields higher normalized scores. For this ablation, GPU Memory is constant across k , so its normalized term is identical for all rows and does not affect the ranking. The overall *Precision-Efficiency Score* is:

$$\text{PES}_k = \frac{1}{4} \left(\text{mIoU}_k^{\text{norm}} + \text{pAcc}_k^{\text{norm}} + \text{Latency}_k^{\text{norm}} + \text{Memory}_k^{\text{norm}} \right). \quad (17)$$

On V21, PES peaks at CG=25, yielding clearly higher mIoU and pAcc compared to 5 or 15 iterations. However, further increasing CG to 35 or 45 brings only marginal accuracy gains while incurring noticeably higher latency, thus reducing the overall PES. We therefore fix the number of CG iterations to 25 for all experiments, as this provides an optimal trade-off between precision and efficiency.

Table B12. **Quantitative results of open-vocabulary semantic segmentation.** “Extra data” denotes external datasets (e.g., CC3M [55], CC12M [11], RedCaps [20], COCO Captions [14, 40], and ImageNet-1K [19]), and “Extra backbone” lists auxiliary models. “Training-free” indicates no extra training. We evaluate prior methods using their default post-processing (official or re-implemented), while reporting PEARL without any post-processing. All metrics are mIoU (%). Best results are highlighted with **bold**, and second best with underlined.

Method	Pub. & Year	Extra data	Extra backbone	Training free	with background			without background				Avg.	
					V21	PC60	Object	V20	PC59	Stuff	City		ADE
<i>w/ Mask Refinement</i>													
GroupViT [69]	CVPR’22	CC12M+RedCaps	✗	✗	51.1	19.0	27.9	81.5	23.8	15.4	11.6	9.4	30.0
TCL [10]	CVPR’23	CC3M+CC12M	✗	✗	55.0	30.4	31.6	83.2	33.9	22.4	24.0	17.1	37.2
CLIP-DINOiser [66]	ECCV’24	ImageNet-1K	DINOv1 (ViT-B/16)	✗	64.6	33.5	36.1	81.5	37.1	25.3	31.5	<u>20.6</u>	41.3
ReCo [57]	NeurIPS’22	ImageNet-1K	✗	✓	27.2	21.9	17.3	62.4	24.7	16.3	22.8	12.4	25.6
FreeDA [4]	CVPR’24	COCO Captions	DINOv2 (ViT-B/14)	✓	52.0	35.2	25.8	79.5	40.2	27.1	34.4	20.9	39.4
LaVG [30]	ECCV’24	✗	DINOv1 (ViT-B/8)	✓	62.1	31.6	34.2	82.5	34.7	23.2	26.2	15.8	38.8
ProxyCLIP* [35]	ECCV’24	✗	DINOv2 [†] (ViT-B/14)	✓	62.0	35.2	38.7	83.1	<u>38.9</u>	<u>26.6</u>	35.4	20.3	42.5
CASS* [32]	CVPR’25	✗	DINOv2 [†] (ViT-B/14)	✓	58.7	32.6	33.3	86.4	35.9	24.0	34.2	17.9	40.4
CASS* [32]	CVPR’25	✗	DINOv3 (ViT-B/16)	✓	62.5	34.5	36.2	87.1	38.2	25.6	37.4	18.9	<u>42.6</u>
MaskCLIP [81]	ECCV’22	✗	✗	✓	37.2	22.6	18.9	72.1	25.3	15.1	11.2	9.0	26.4
SCLIP* [62]	ECCV’24	✗	✗	✓	61.7	31.5	32.1	83.5	36.1	23.9	34.1	17.8	40.1
NACLIP* [26]	WACV’25	✗	✗	✓	<u>64.1</u>	35.0	36.2	83.0	38.4	25.7	38.3	19.1	42.5
SFP* [28]	ICCV’25	✗	✗	✓	58.8	34.3	34.9	85.1	38.3	25.9	36.0	19.4	41.6
<i>w/o Mask Refinement</i>													
PEARL (Ours)		✗	✗	✓	<u>64.1</u>	<u>35.1</u>	<u>37.3</u>	<u>86.9</u>	38.6	26.3	37.6	19.4	43.2

Notes: “*” denotes performance reproduced in this work. “†” indicates DINOv2 with registers [18].

C. More Quantitative Results

Table B12 presents a quantitative comparison with recent open-vocabulary semantic segmentation methods. For all comparison baselines, we keep their default post-processing (e.g., PAMR [1] or DenseCRF [34]), while PEARL is evaluated with CLIP ViT-B/16 only and *without* any mask refinement. Even in this setting, PEARL achieves the highest average mIoU of **43.2%** across the eight benchmarks. It surpasses the strongest baseline, CASS [32] with DINOv3 (42.6%), by **0.6** points and outperforms other training-free CLIP-based methods, such as NACLIP [26] (42.5%) and SFP [28] (41.6%). This demonstrates that our alignment and propagation modules provide clear improvements without relying on stronger backbones or extra training data.

D. More Qualitative Results

As illustrated in Figs. D6-D13, we provide additional qualitative results of our PEARL on all eight benchmarks: Pascal VOC 21 (**V21**) [23], Pascal Context 60 (**PC60**) [44], COCO-Object (**Object**) [40], Pascal VOC 20 (**V20**) [23], Pascal Context 59 (**PC59**) [44], COCO-Stuff (**Stuff**) [8], Cityscapes (**City**) [17], and ADE20K (**ADE**) [79]. These examples include both successes and typical failure cases.

For each example, we show the input (**Image**), our prediction (**PEARL**), and the ground-truth (**GT**) mask. All visualizations utilize CLIP ViT-B/16 as the vision backbone, and no post-processing (e.g., PAMR [1] or DenseCRF [34]) is applied. Therefore, the masks directly reflect the behavior of our training-free pipeline. On V21/V20 [23]

and PC60/PC59 [44], our PEARL produces accurate object extents and clean boundaries for a wide variety of categories, including animals, vehicles, and artificial objects. The method remains robust under large appearance changes (e.g., illumination and pose) and complex foreground-background compositions, and it preserves small details such as thin structures and disconnected parts in many cases. On the Object [40] and Stuff [8] datasets, our PEARL can localize both foreground instances and amorphous “*stuff*” regions, showing that the proposed Procrustes alignment and text-aware propagation generalize well from object-centric images to more cluttered scenes.

For the more challenging City [17] and ADE [79] benchmarks, our PEARL still captures the dominant layouts and most large regions (*road, building, sky, vegetation, cars*), but some fine-grained structures and rare categories are not perfectly segmented. The failure cases in figures mainly fall into several patterns: boundary leakage between adjacent regions, missing or fragmented small objects, and confusion between semantically related classes under cluttered scenes or weak visual evidence. These failure modes highlight the remaining gap between current open-vocabulary semantic segmentation and fully supervised models on large-scale, high-resolution urban or scene parsing datasets: long-range context, small distant objects, and heavily overlapping classes remain difficult to resolve using frozen backbones and text prompts alone. We hope that these visualizations will motivate future work on stronger open-vocabulary priors and the better exploitation of geometric and contextual cues in complex, real-world scenes.



Figure D6. **Qualitative results of open-vocabulary semantic segmentation.** Results are shown on the V21 [23] dataset. Our PEARL use CLIP ViT-B/16 [51], and no post-processing (e.g., PAMR [1] or DenseCRF [34]) is applied for a fair comparison.

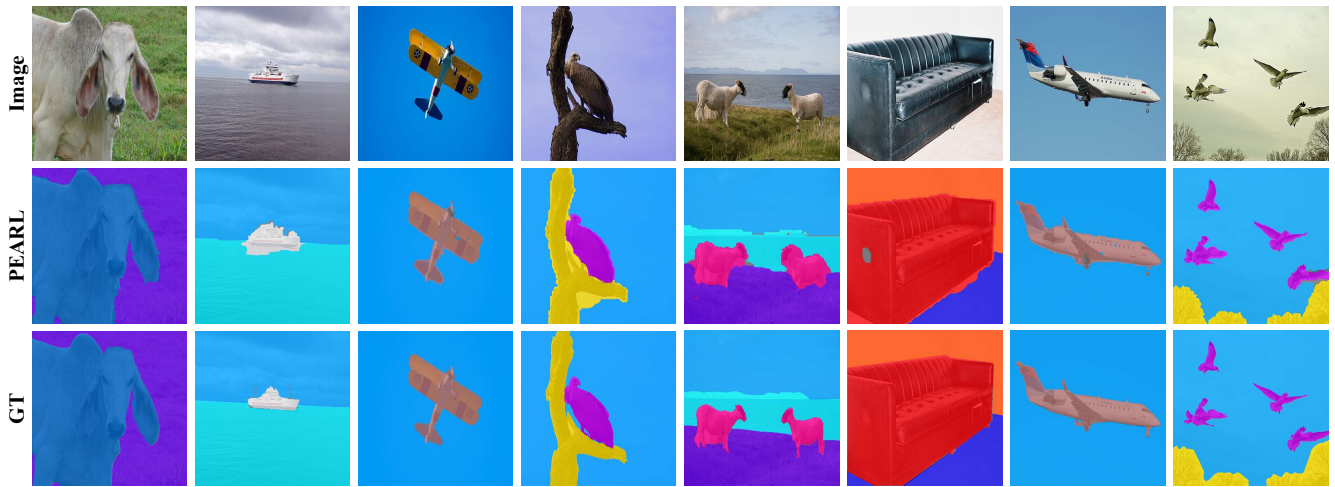


Figure D7. **Qualitative results of open-vocabulary semantic segmentation.** Results are shown on the PC60 [44] dataset. Our PEARL use CLIP ViT-B/16 [51], and no post-processing (e.g., PAMR [1] or DenseCRF [34]) is applied for a fair comparison.

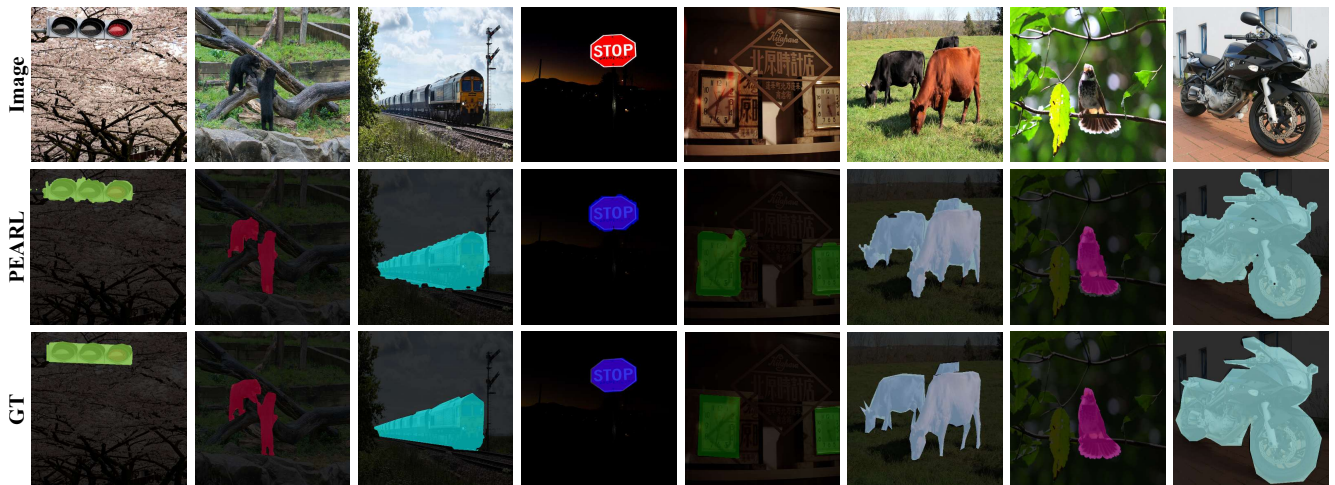


Figure D8. **Qualitative results of open-vocabulary semantic segmentation.** Results are shown on the Object [40] dataset. Our PEARL use CLIP ViT-B/16 [51], and no post-processing (e.g., PAMR [1] or DenseCRF [34]) is applied for a fair comparison.



Figure D9. **Qualitative results of open-vocabulary semantic segmentation.** Results are shown on the V20 [23] dataset. Our PEARL use CLIP ViT-B/16 [51], and no post-processing (e.g., PAMR [1] or DenseCRF [34]) is applied for a fair comparison.



Figure D10. **Qualitative results of open-vocabulary semantic segmentation.** Results are shown on the PC59 [44] dataset. Our PEARL use CLIP ViT-B/16 [51], and no post-processing (e.g., PAMR [1] or DenseCRF [34]) is applied for a fair comparison.

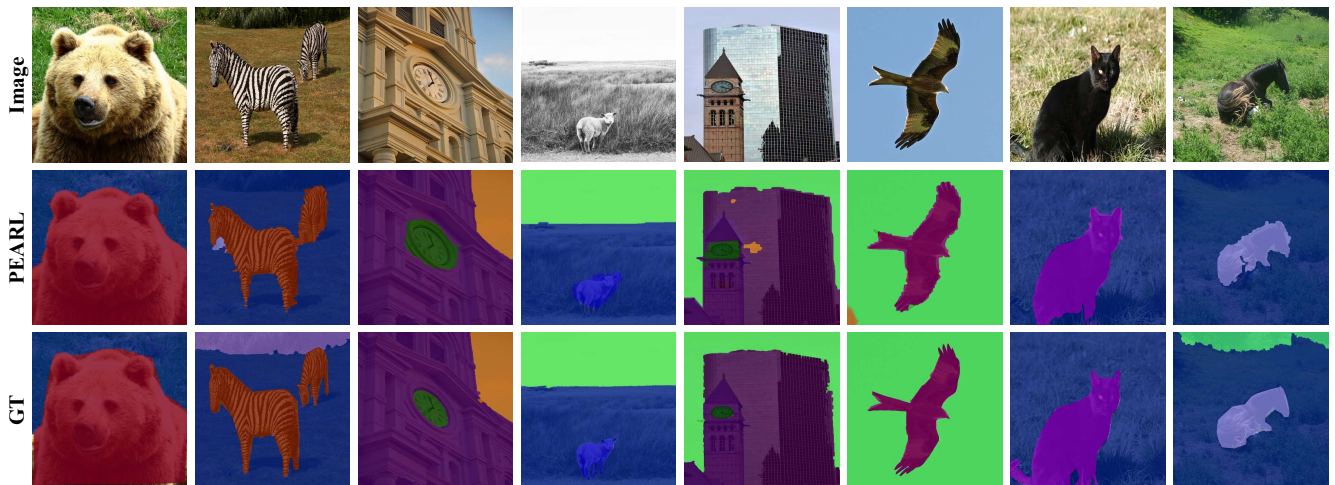


Figure D11. **Qualitative results of open-vocabulary semantic segmentation.** Results are shown on the Stuff [8] dataset. Our PEARL use CLIP ViT-B/16 [51], and no post-processing (e.g., PAMR [1] or DenseCRF [34]) is applied for a fair comparison.

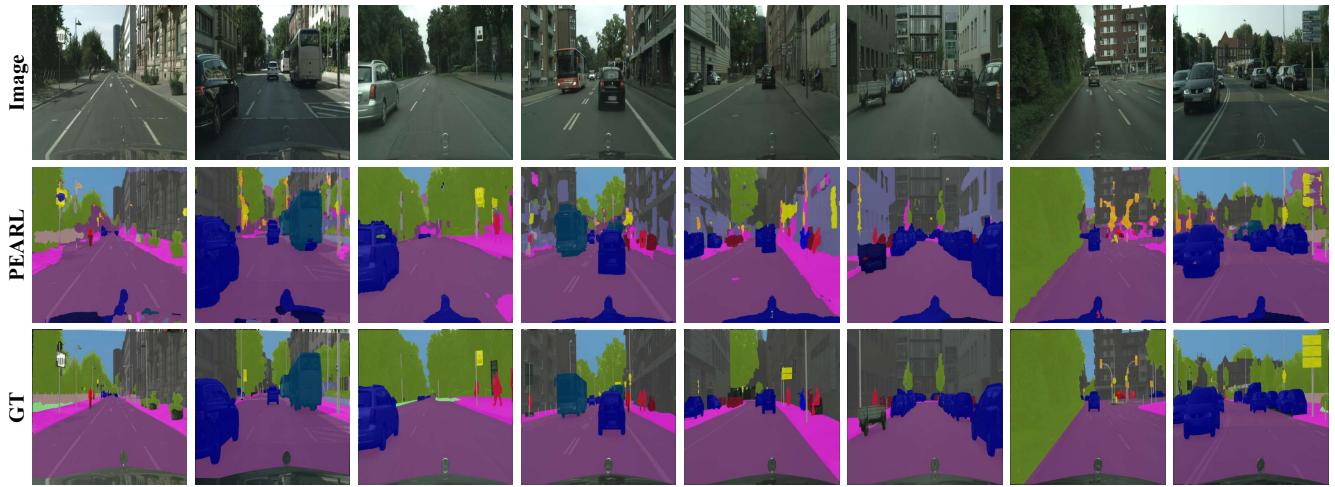


Figure D12. **Qualitative results of open-vocabulary semantic segmentation.** Results are shown on the City [17] dataset. Our PEARL use CLIP ViT-B/16 [51], and no post-processing (*e.g.*, PAMR [1] or DenseCRF [34]) is applied for a fair comparison.

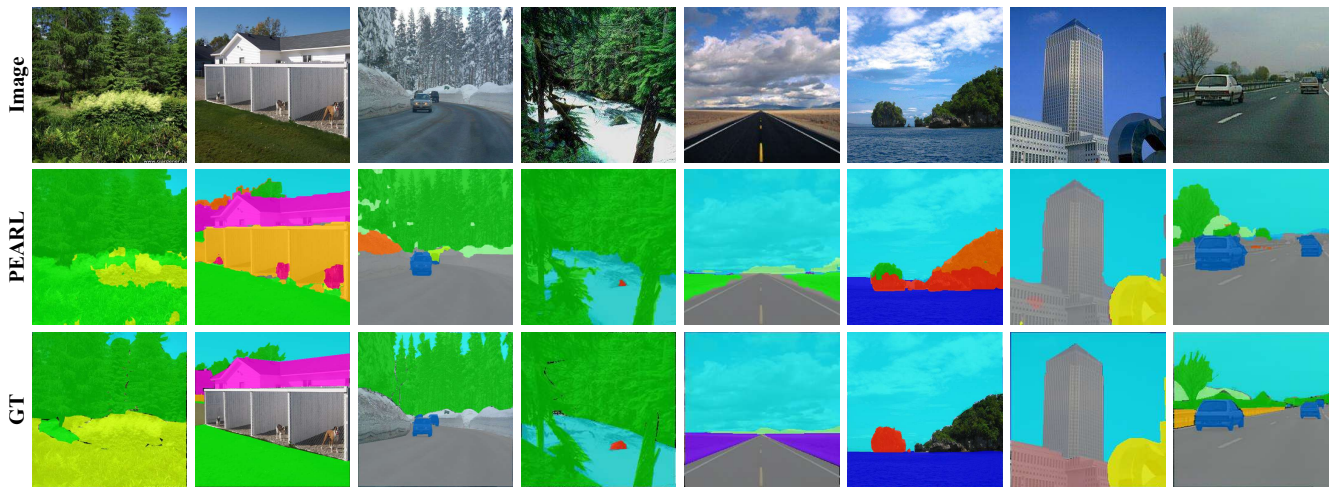


Figure D13. **Qualitative results of open-vocabulary semantic segmentation.** Results are shown on the ADE [79] dataset. Our PEARL use CLIP ViT-B/16 [51], and no post-processing (*e.g.*, PAMR [1] or DenseCRF [34]) is applied for a fair comparison.